Study and optimization of epitaxial films of Cr and Pt/Cr bilayers on MgO

C. Rinaldi[1,2], M. Asa[1], D. Chrastina[1], J. L. Hart[3,4], M. L. Taheri[3,4], I. Pallecchi[5], D. Marré[5], and M. Cantoni[1]

[1] *Dipartimento di Fisica, Politecnico di Milano, p.zza L. da Vinci 32, 20131 Milano, Italy*

[2] *IFN-CNR, Institute of Photonics and Nanotechnologies, piazza Leonardo da Vinci 32, 20133 Milano, Italy*

[3] *Department of Materials Science and Engineering, Drexel University, 3141 Chestnut Street, Philadelphia PA, 19104, USA*

[4] *Department of Materials Science and Engineering, Johns Hopkins University, Whiting School of Engineering, 3400 North Charles Street, Baltimore, Maryland, 21218, USA*

[5] *CNR-SPIN, C/o Dipartimento di Fisica, University of Genoa, Via Dodecaneso 33, Genova, 16146, Italy*

ABSTRACT

We report a systematic study of the fabrication and chemical and structural characterization of epitaxial Cr films and Pt/Cr bilayers on MgO substrates. Cr films of different thicknesses were grown by molecular beam epitaxy at 373 K and then post-annealed at different temperatures. These films are chemically stable, present a well-ordered tetragonal structure, with only a low degree of oxidation distributed throughout the films. The lattice parameter can be finely tuned by varying the film thickness and the post-annealing temperature, as the elastic energy is progressively relaxed by edge dislocations, so that the film can approach the structural and electrical properties of bulk chromium. Moreover, the chemical and structural properties of Cr are not affected by a Pt capping layer, which grows in a well-ordered Pt[110]||Cr[100] orientation, holding potential for applications in recently proposed Pt/Cr-based antiferromagnet spintronics and for the realization of epitaxial Pt films on MgO by using a thin buffer layer of chromium.

1. INTRODUCTION

While antiferromagnets have historically been employed as passive elements in magnetic junctions, they have only recently started to play an active role in antiferromagnetic (AFM) spintronic devices [1]. AFM materials do not produce stray magnetic fields, are invisible to external magnetic probes, are robust against external unintended magnetic fields and have typical precession frequencies in the THz range [1,2,3]. These properties make them good candidates for different applications, from information storage to spin-currents operation. The former is definitely the most investigated, in the search for a new generation of magnetic memories (MRAMs) with improved robustness and scalability [4]. Different approaches for storing and reading information in the spin configuration of an AFM layer have been explored [5]. Information storage can be achieved by exchange spring with a FM layer [6], field-cooling [7], strain [8], current-induced torques [9], magneto-electric effects [10], or mechanisms based on the spin Hall Effect [11]. To read the information, anisotropic magneto resistance (AMR) effects in thin films [12] or vertical devices comprising a tunnel barrier [7,13] may be exploited. Different conducting materials have been investigated for AFM spintronic applications, such as FeRh [12], IrMn [13,14,15], Mn_2Au [16,17], CuMnAs [18,19], Sr_2IrO_4 [20], and Cr [21,22].

Chromium is very appealing for several reasons. It is a widely employed 3d-metal, relatively abundant on earth [23], and the only elemental antiferromagnet at room temperature, with a bulk Néel temperature of 311 K and a complex magnetic behavior comprising commensurate and incommensurate spin density wave antiferromagnetism [22, 24]. AMR in bulk Cr, i.e. the dependence of the electrical resistivity on the relative direction between current and spin, has been demonstrated [21] and enables retrieval of the AFM state. Chromium thin films are definitely easier to prepare than binary or ternary compounds (such as Mn_2Au, IrMn, CuMnAs), because there is no need to satisfy stoichiometry constraints to obtain the AFM phase. Epitaxial single crystals can be obtained using molecular-beam epitaxy (MBE) [25,26] or magnetron sputtering [27] on top of

several metals (e.g., Au [28], Ag [29], and Fe [30]) and oxides (e.g., MgO [31], $SrTiO_3$ [32], TiO_2 [33], and Al_2O_3 [34]). The structural and transport properties of thin epitaxial films have been addressed by different techniques (see, e.g., the synchrotron-based studies of charge-density, strain and spin-density waves reported in Refs. [35] and [36]). Magneto-transport studies on Cr epitaxial films have been reported [37, 38], also by some of the authors [39]. Finally, chromium films may also be suitable for the realization of complex fully epitaxial heterostructures, allowing the exploitation of symmetry filtering effects in epitaxial metal/oxide stacks. In fact, epitaxial Pt/Cr/MgO heterostructures have been recently predicted to develop an overall spin polarization and to present anisotropic magneto resistance effects [40].

Following the idea of using Pt/Cr heterostructures for spintronic applications, in this work we systematically study the growth of Cr thin films and Pt/Cr bilayers on MgO(001) substrates. The film quality is assessed as a function of different parameters (layer thickness and preparation procedure), in terms of structural, chemical, and electrical properties. We aim to demonstrate the growth of Cr thin films with structural and chemical quality comparable to bulk. Moreover, the novelty of the work lies in the tunability of the chromium lattice parameter versus thickness (2-50 nm) and thermal annealing (from RT up to about 870 K). Such tunability and control of the chromium quality is also the starting point for the deployment of epitaxial Pt(~ 3 nm)/Cr heterostructures for spintronic devices [40]. We showed that, while the direct deposition of Pt on MgO requires high substrate temperatures (> 500 °C) to promote a "cube-on-cube" growth in the Volmer-Weber mode [41], the use of high quality thin Cr as interfacial layer between Pt and MgO enables high quality Pt layers with single epitaxial orientation. Noteworthy, the immediate outcome of this work has been the measurement of the anomalous Hall effect (AHE) in Pt/Cr/MgO heterostructures [39], grown according to the procedure here reported. AHE proves the existence of an out-of-plane magnetization in such heterostructures, induced by magnetic proximity effect at the Pt/Cr interface, as well as its dependence only on the field cooling direction and its insensitivity to

the magnetic field below the Néel temperature [39]. MgO was selected as substrate since the lattice mismatch between MgO(001) and Cr can be as small as 3.2%, assuming an in-plane rotation of 45°, with respect to the cube-on-cube growth (Cr[110] parallel to MgO[100]). Moreover, the Cr/MgO interface has been proven to be stable against oxidation [25] and, being insulating, MgO allows to measure the electric properties of the conductive epilayers (AMR, Hall effect, …).

2. EXPERIMENTAL

MgO(001) substrates were cleaned by isopropanol and deionized water, then annealed in ultra-high vacuum (UHV, chamber pressure $<10^{-9}$ mbar) at 900 K for 2 hours. Cr and Pt were deposited by MBE at about 0.3 nm/min, as checked by a quartz microbalance. The substrate was kept at 373 K during Cr deposition [31], whereas Pt was grown at room temperature (RT). Prior to Pt deposition, post-annealing was performed on selected Cr films at different temperatures (523 K, 873 K). The list of Cr/MgO samples considered in this work is reported in Table I. We adopted the following convention for the sample names, in order to underline the differences between them: (i) the first letter indicates the stack (C is Cr uncapped, P is Pt/Cr); (ii) the subsequent number is the Cr thickness in nanometers; (iii) the last letter indicates the post annealing conditions of Cr (no letter means no post-annealing, while "a" and "A" mean post-annealing at 523 K and 873 K, respectively). The growth was performed in a UHV cluster tool allowing for *in-situ* substrate cleaning, sample growth by MBE and characterization by electron diffraction and photoelectron spectroscopy techniques, as described in detail elsewhere [42]. In particular, the chemical and structural properties of Cr films and heterostructures were investigated *in-situ* by X-ray Photoemission Spectroscopy (XPS), X-ray Photoemission Diffraction (XPD), and Low Energy Electron Diffraction (LEED). Photoelectrons in XPS and XPD were excited by standard Al-Kα X-ray source and collected by a Hemispherical Energy Analyzer (HEA) Phoibos 150 (SPECS™),

yielding an acceptance angle of ±2.5°, a field view of ~1.4 mm^2 and an energy resolution of 0.95 eV.

Sample	Cr thickness (nm)	Cr post-annealing temperature (K)	Pt thickness (nm)
Cref	10	/	/
C2	2	/	/
C2A	2	873	/
C10	10	/	/
C25	25	/	/
C50	50	/	/
C50a	50	523	/
C50A	50	873	/
P2A	2	873	3
P10	10	/	3
P50	50	/	3
P50A	50	873	3

Table I. List of Cr/MgO and Pt/Cr/MgO samples employed. All the samples, apart from the reference (Cref), were grown keeping the substrate temperature at 373 K. In the sample names, the first letter indicates the stack (C is Cr uncapped, P is Pt/Cr), the number is the Cr thickness in nanometers. The last letter indicates the post-annealing conditions (no letter means no post-annealing, while “a” and “A” mean post-annealing at 523 K and 873 K, respectively).

X-ray diffraction (XRD) was carried out using a PANalytical X’Pert PRO high-resolution diffractometer. The Kα1 radiation from the Cu anode (λ = 0.15406 nm) was selected using a hybrid mirror and 2-bounce Ge monochromator. The sample was mounted on a high-precision goniometer with translational (x, y and z) and rotational (incidence angle ω, diffraction angle 2θ, sample rotation φ and sample tilt χ) degrees of freedom. A three-bounce Ge monochromator was placed in front of the detector as an analyser crystal, in order to obtain high precision in 2θ and to reject fluorescence

from the sample. By manual alignment and reciprocal space mapping, MgO(004) and Cr(002) peak positions were found in the symmetrical ($\omega \approx 2\theta/2$) scattering geometry, and MgO(024) and Cr(112) peak positions were found in the asymmetrical grazing-incidence geometry ($0 < \omega < 2\theta/2$). The measured in-plane ($a_{//}$) and out-of-plane ($a_{\perp}$) lattice parameters of the Cr film were checked to be consistent with the bulk unstrained lattice parameter (a_{bulk}) according to the RT elastic constants from Bolef and de Klerk [43].

High-resolution transmission electron microscopy (HR-TEM) was performed using a JEOL 2100F (Schottky source) microscope. The sample was prepared via mechanical polishing and ion milling. Final milling was performed with 3 keV Ar ions. The oxidation state of the Cr film was studied with STEM and direct detection (DD) EELS [44]. For EELS, a dispersion of 0.125 eV/channel was used with a collection semi-angle of 30 mrad.

Electrical resistivity measurements by four-probe technique were performed in Physical Properties Measurement System (PPMS) by Quantum Design at temperatures from 380 K to 5 K.

3. CHROMIUM THIN FILMS: STRUCTURAL AND CHEMICAL PROPERTIES

A. Chemical stability and oxidation

Figure 1 reports the XPS spectra of the Cr $2p_{3/2}$ core level, at normal incidence and after subtraction of a Shirley background due to inelastic electron scattering. Such spectra were acquired: (i) Cr(2 nm)/MgO(001) as-grown (C2) and (ii) post-annealed (C2A), (iii) Cr(50 nm)/MgO(001) post-annealed (C50A), and (iv) a reference metallic Cr film (Cref). The latter was grown by MBE at room temperature on a MgO substrate, and not annealed in order to preserve Cr purity excluding any temperature-induced oxidation and/or interdiffusion. The oxygen content was well below the experimental XPS accuracy (<1%), indicating the absence of any chromium oxide in the reference sample. The peak position is the same for all the spectra (574.4±0.1 eV, coherent with the tabulated

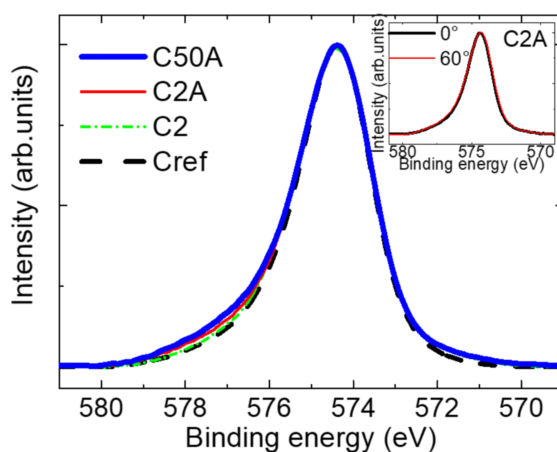

Fig. 1. XPS spectra of the Cr $2p_{3/2}$ core level, measured at normal incidence on samples C50A (blue thick line), C2A (red thin line), C2 (green dashed-dotted line), and Cref (dashed black line). The intensity scale was renormalized for each spectrum to the peak height. The inset shows the XPS spectra of the C2A sample taken at normal incidence (black thick line) and grazing incidence (red thin line), corresponding to polar angles of 0° and 60° respectively.

value for metallic Cr [45]), while the shoulders on the higher BE side of the peaks suggest a relatively low degree of oxidation which increases with annealing and thickness. The same conclusion comes out from the EELS (see Supplementary Information S1), which measured an atomic oxygen content of roughly 3% in the C50A Cr film, mostly constant across the Cr film thickness, which could be due to surface oxidation of the TEM specimen during preparation. In the inset of Fig. 1 we report the Cr $2p_{3/2}$ spectra of sample C2A at two different take-off angles of photoelectrons with respect to the surface normal, 0° (normal emission) and 60° (grazing emission). The electron escape depth of the Cr $2p_{3/2}$ photoelectrons is about 1.54 nm [46], yielding a probing depth of few nanometers. No difference can be noticed between the spectra, despite the different sensitivity of the two experimental configurations (grazing vs. normal incidence), thus excluding any relevant surface or interface O concentration. We can conclude that a negligible amount of

oxygen is distributed within the Cr film. This can be justified by the chemical and physical stability of MgO in contact with 3d metals [46], at variance with other oxides such as BaTiO3 [47], because of its large negative Gibbs energy of formation.

B. Structure and morphology

Figure 2(a) reports the XPD pattern from sample C50A along the [110] azimuth of MgO, obtained measuring photo-electrons coming from Cr $2p_{3/2}$ core level excited by Al-Kα X-ray source. At this stage, the characterization was performed by photoelectron diffraction. The in-situ technique guarantees direct comparison between virgin and annealed samples without exposure to air. Moreover, XPD is suitable for the study of ultrathin films (not accessible by XRD) and is chemically selective, i.e. has the possibility to probe the crystal structure around a given element within the same template (for example, see the Pt/Cr bilayer in Sect. 4). The two main peaks at 28°±1° and 45°±1° can be ascribed to the diffraction. These angles correspond to the directions characterized by the maximum atomic density, as expected by the diffraction in forward scattering regime. The inset shows the atomic arrangement in the (010) plane of a bcc crystal and demonstrates that these directions correspond precisely to the [102] and [101] of a bcc Cr (dashed lines) with [100] azimuth [48]. It makes clear that a 45° rotation between the Cr and MgO lattices in the (001) plane occurs, to minimize the lattice mismatch (3.2% in the Cr[110]||MgO[100] configuration, assuming the bulk values of the lattice parameters). The quality of the XPD pattern with the peaks clearly emerging from background reflects the good crystal quality of Cr films, as also confirmed by LEED (see Supplementary Information S2).

The morphology of the film was measured by atomic force microscopy and reported in Fig. 2(b). The sample is atomically flat with a roughness of 0.3 nm (RMS). The annealing doesn't produce differences in morphology and roughness as compared to the surface without annealing (see Supplementary Information S3).

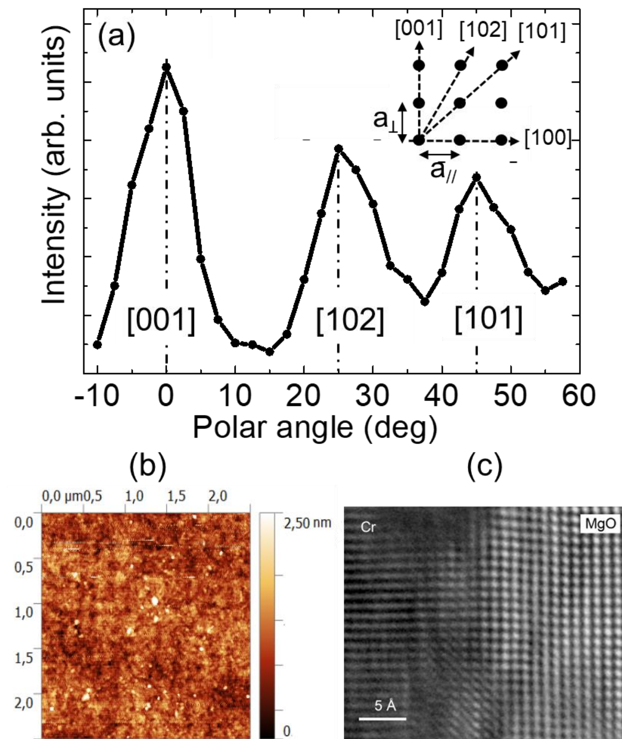

Fig. 2. Sample C50A: (a) XPD pattern of the Cr $2p_{3/2}$ core level along the MgO [110] azimuth on sample C50A. In the inset is reported the atomic arrangement of a tetragonal lattice in the (010) plane, with the main diffraction directions indicated. (b) Atomic force microscopy image of a 2.5µm×2.5µm sample area. (c) Fourier-filtered HR-TEM in the (010) MgO plane, corresponding to the $(1\bar{1}0)$ Cr plane.

Fig. 2(c) reports a HR-TEM image of the Cr/MgO interface in the (010) MgO plane for C50A. The TEM shows for Cr the $(1\bar{1}0)$ cross section and a single crystal with a cubic structure. The measured spacing between adjacent atomic planes from selected area electron diffraction are 0.409±0.002 nm along Cr[110] and 0.287±0.002 nm along Cr[001]. The corresponding in-plane ($a_{//}$) and out-of-plane ($a_{\perp}$) lattice parameters of the Cr primitive cell, averaged through the film thickness,

are 0.289±0.003 nm (calculated as the measured spacing along [110] divided by $\sqrt{2}$) and 0.287±0.003 nm, respectively. They fit reasonably with the nominal lattice parameter of the cubic cell (0.2885 nm),[26] demonstrating that the C50A film is very similar to a bulk Cr single crystal. This is crucial in view of applications pointing to the realization of thin films to be used in integrated devices, with nominally the same structural properties of bulk Cr single crystal elements [21].

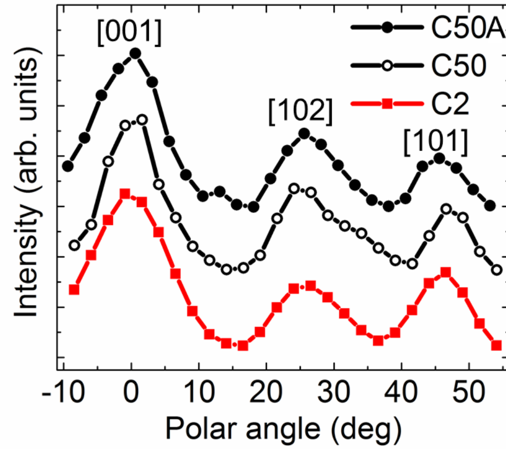

Fig. 3. XPD pattern of the $Cr2p_{3/2}$ core level along the MgO [110] azimuth on samples with C2 (red squares), C50 (black empty dots) and C50A (black dots) structures.

C. Film thickness and post-annealing temperature

We now consider the effects of film thickness and the post-annealing temperature on the structure of Cr films. Fig. 3 reports the XPD patterns along the MgO [110] azimuth for C2 (red squares), C50 (black empty dots) and C50A (black full dots) samples [49]. Quite surprisingly, all the XPD patterns have well defined peaks along the expected diffraction directions [see also Fig. 2(a)].

Note that the [101] diffraction peak of C2 (red line) at 46.5° fits with the substrate-matching situation. This can be understood looking at the inset of Fig. 2(a). The polar angle along the [110] direction (that is the angle between the [110] and [001] directions) is given by arctan($a_{//}/a_{\perp}$). For a

cubic lattice we have $a_{//}/a_{\perp} = 1$ and thus the diffraction angle is 45°. In case of a perfect in-plane matching with the MgO substrate, instead, the Cr cell will be tetragonal: $a_{//}$ will fit the MgO in-plane lattice parameter, divided by $\sqrt{2}$ because of the Cr[100]||MgO[110] epitaxial relationship, which is $a_{//} = 0.2978$ nm. Assuming the Poisson ratio of 0.1622 [43], $a_{\perp}$ will be 0.2849 nm instead. We thus have $a_{//}/a_{\perp} = 1.05$ and a diffraction angle of about 46.3°.

The reduced thickness of the C2 sample determines an in-plane tensile strain ($a_{//}/a_{\perp} = 1.05$). The situation is unchanged in C50, whereas in C50A the peak moves towards the value expected for bulk Cr. The same behavior happens in C2A too (the [101] peak moves to 45.8°, corresponding to $a_{//}/a_{\perp} \approx 1.03$, data not shown). Anyway, a full relaxation in such a thin film should be excluded, even at larger annealing temperatures, because of the relevant, and unavoidable, contribution to lattice distortion due to the mismatch at the interface. Apart from elastic energy relaxation, the crystal structure of these Cr films is the same for all the post-annealing temperatures. The stability of the Cr layers structure makes particularly appealing the use of the Cr film as a seed layer for the growth of additional layers, whose preparation could require specific post-annealing treatments, as in the case of heavy metals such as Pt (see the next section) or insulating films such as MgO (see Supplementary Information S2).

In order to gain structural information on the full film thickness (XPD is limited to a few nanometers by the photoelectron escape depth [46]) concerning the strain versus thickness and thermal treatment, XRD was performed on a set of selected samples. Figure 4(a) show the measured in-plane ($a_{//}$) and out-of-plane ($a_{\perp}$) lattice parameters of as-grown Cr films as a function of the thickness (C10, C25, C50, and duplicates, for improving the statistics). An almost linear dependence with film thickness is evident, with $a_{//}$ decreasing and $a_{\perp}$ increasing towards the nominal lattice parameter for the cubic Cr cell ($\bar{a} = 0.2885$ nm).

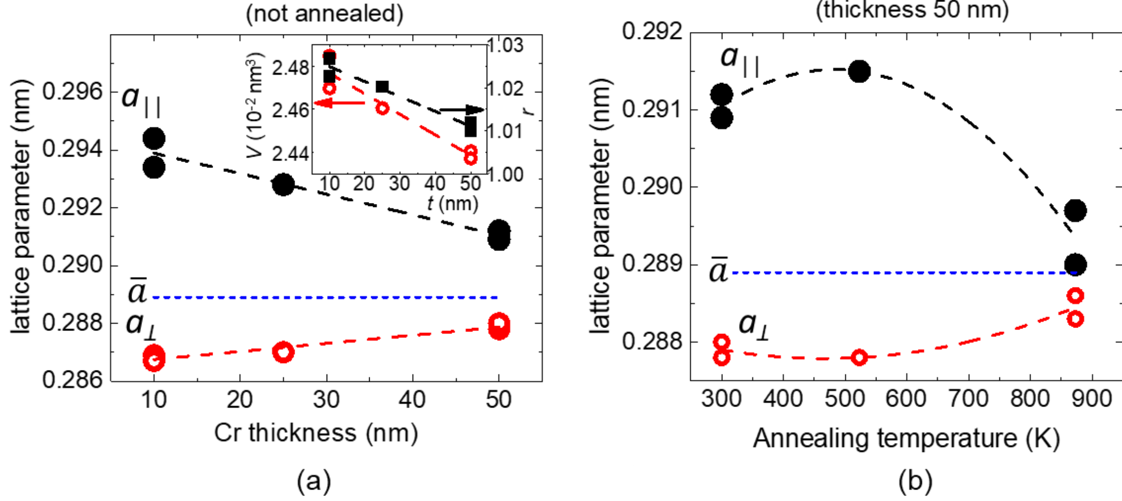

Fig. 4. (a) In-plane ($a_{//}$, black full dots) and out out-of-plane ($a_\perp$, red empty dots) lattice parameters of as-grown Cr films as a function of thickness, compared with the nominal value ($\bar{a}$, blue dashed line). In the inset, the cell volume V (red empty dots) and the ratio $r = a_{//}/a_\perp$ for the films (black full squares) are reported. (b) $a_{//}$ and $a_\perp$ lattice parameters of 50 nm thick Cr films as a function of the post-annealing temperature.

The bulk value is however not achieved for any of the non-annealed films reported in Fig. 4(a): all of them present tetragonal cells with in-plane tensile strain ($a_{||}/a_\perp > 1.01$). Figure 4(a) reports the cell volume V (red empty dots, scale on the left) and the ratio $r = a_{//}/a_\perp$ (black full squares, scale on the right) as a function of the Cr thickness: the former decreases and the latter increases, when films become thicker, towards the bulk condition ($V = 2.41\times10^{-2}$ nm^3, $r = 1$). Note that the MgO lattice parameter divided by $\sqrt{2}$ is 0.2982 nm, larger than $a_{//}$: as discussed above, even for low thickness, these films are partially relaxed with respect to the substrate.

The effect of the annealing temperature is illustrated in Fig. 4(b) for a 50 nm thick Cr film. The error bar can be estimated as the lattice parameter difference between the two nominally identical C50 samples (0.0004 nm). While the annealing shows almost no effect up to 523 K (C50a), being

the lattice variation inside the error bar, at 873 K (C50A) the Cr cell clearly releases its tetragonal deformation and becomes almost cubic, approaching the lattice parameter of bulk Cr as already shown by TEM. This behavior can be justified by the introduction of misfit dislocations, that move to the film/substrate interface at which they can relax the greatest thickness of film, in order to maximize the release of strain energy. For this reason, no strain gradient from the interface to the surface are present in thin films of a constant composition (see Supplementary Information S4 and S5). As noted above, the structurally fully equivalence to bulk single crystals of Cr thin films (50 nm thick), grown under appropriate conditions (growth temperature of 373 K, annealing temperature of 873 K), is a very relevant result. On the other hand, the stress control in the Cr film via thickness and/or annealing temperature can be potentially exploited to tune the Néel temperature, extending the device capability to different temperature ranges [50,51]. A Néel temperature variation of about 100 K has been measured, from 290 K to below 200 K upon the increase of the Cr thickness from 25 to 50 nm (or 75 nm). For more detail see Ref. [39].

4. Pt/Cr BILAYERS

For the past few years, Pt has played a relevant role in spintronics, acting as a non-magnetic layer in spin-orbit-torque (SOT) devices with FMs [52,53]. Proximity effects [54] and spin Hall magnetoresistance [55] have also been reported for different Pt/AFM systems.

Here we explore the chemical, structural and transport properties of 3 nm thick Pt films on top of the Cr layers studied in the previous section. The bulk lattice parameters are 0.2885 nm and 0.3912 nm for Cr[100] and Pt[100], respectively. An epitaxial relationship is thus established provided that Pt and Cr lattices are rotated by 45°, with Cr[100] parallel to Pt[110], in order to reduce the lattice mismatch (4.1% between Cr[100] and Pt[110]). For comparison with uncapped films, four Pt-capped samples were fabricated, called P2A, P10, P50 and P50A (see Table I). They correspond to C2A, C10, C50 and C50A samples, respectively, with the addition of 3 nm of Pt on

top, grown *in-situ* by MBE at RT and without any post-annealing treatment.

XPS on the 2 nm thick Cr film (P2A) does not show any trace of chemical shift in the Cr $2p_{3/2}$ core peak (see Supplementary Information S6). The structural characterization of Cr and Pt/Cr films was performed *in-situ* exploiting the chemical selectivity of the X-ray Photoelectrons Diffraction (XPD), which enables the investigation of the surroundings of a given atomic species.

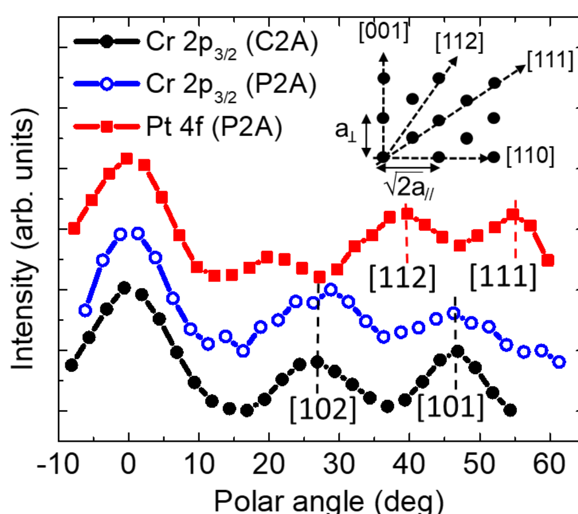

Fig. 5. XPD pattern of the Cr $2p_{3/2}$ (black and blue curves) and Pt 4f (top, red line) along the MgO [110] azimuth on samples C2A and P2A. Dashed lines indicate the main diffraction peaks, [102] and [101] for Cr (black line), [112] and [111] for Pt (red lines), respectively. In the inset is reported the atomic arrangement of a tetragonal lattice in the $(1\bar{1}0)$ plane, with the main diffraction directions indicated.

Indeed, the analysis of elastically scattered electrons from Cr $2p_{3/2}$ and Pt 4f core levels permits to investigate the crystallographic structure and order of Cr and Pt lattices. The result is shown in Fig. 5, where the polar scans of Cr $2p_{3/2}$ are collected on the uncapped and Pt-capped films, and he Pt 4f peak on the Pt capping layer. The well-defined diffraction peaks of all the scans demonstrate the good crystal quality of both Cr and Pt. Moreover, the quality of XRD on Cr films is maintained

upon Pt deposition [56], suggesting once more that the Cr crystal order is preserved and ruling out a significant intermixing, and the Pt layer itself is highly ordered. The diffraction pattern from Pt 4f photo-emitted electrons along the MgO [110] azimuth shows two main peaks at about 39.0° and 54.8° polar angles, which can be ascribed to diffractions along the Pt [112] and Pt [111] directions, respectively (see the atomic arrangement of a tetragonal lattice in the $(1\bar{1}0)$ plane, shown in the inset, with the main diffraction directions indicated), confirming the 45° rotation between Pt and Cr to minimize the lattice mismatch (see Supplementary Information S7). Finally, the sample was post-annealed at 473 K in order to test the thermal stability. No sizable modification was detected either in XPS or XPD patterns (data not shown), indicating that the Pt crystal structure and quality are already established during the film growth. Also the morphology is not affected by the annealing and is consistent with the uncapped Cr surface (roughness of 0.3 nm, estimated by X-ray reflectivity, data not shown).

5. ELECTRICAL CHARACTERIZATION

Figure 6 reports the resistivity versus temperature for P10 and P50 samples. At fixed *T*, the resistivity decreases as the film thickness increases (from 43.7 μΩ cm for P10 to 29.2 μΩ cm for P50, at RT) [57]. This tendency can be related to the contribution from the interfaces, that becomes more relevant when the film thickness decreases, and/or to the ordering of the Cr film, that improves with the thickness (see Sect. 3C). Indeed, the resistivity further drops in P50A (13.1 μΩ cm at RT), fully relaxed and quite similar to a single crystal in terms of lattice parameters. Also, the resistivity value is fully compatible with single crystal films [38]. The ratio R(300 K)/R(10 K), is about 1.8 for all samples. This quite small value is indicative of the presence of scattering sources (defects, impurities, …), likely concentrated at the interfaces, because no dependence on the Cr thickness or annealing conditions is evident in the R(300 K)/R(10 K) value.

Thus, we demonstrated that epitaxial Pt thin films can be grown on Cr(001), realizing a top conducting layer where electrically-based writing and reading of the spin information in Cr can be tested (e.g., the measurements of magnetic proximity effects in Pt/Cr system reported in Ref. [39]).

As mentioned above, the epitaxial Pt/Cr heterostructure has been successfully employed for demonstrating by Anomalous Hall Effect the existence of an out-of-plane magnetization, which depends only on the field cooling direction and is insensitive to the magnetic field below the Néel temperature, clearly indicating its AFM origin [39]. On the other hand, it has also been proven (see, e.g., Ref. [31] and Supplementary Information S2) that an epitaxial insulating MgO layer can be realized on Cr. This layer has been employed as tunnel barrier in vertical devices and has been demonstrated to influence the spin-density wave transport in Cr/MgO [25] and Cr/MgO/Cr [31] epitaxial systems. M. Bragato *et al.* [40] recently discussed the opportunity of using a nano-sized epitaxial Pt/Cr/MgO/Pt template as a memory cell exploiting the AMR effect [7]. These considerations indicate the strong potential of Cr to support epitaxial layers and/or stacks on top, and once more underline its potential for AFM spintronics applications.

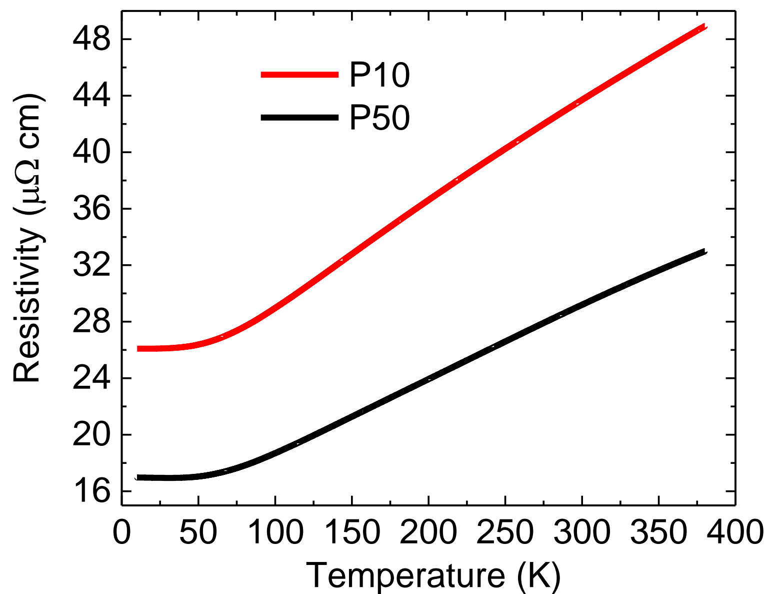

Fig. 6. Resistivity vs T curve of P10 (red) and P50 (black) samples.

6. CONCLUSIONS

In this paper we discussed the growth and the chemical and structural characterization of chromium films and Pt/Cr bilayers on MgO(001) substrates. Cr films were grown by molecular beam epitaxy and post-annealed at different temperatures. MgO is chemically stable and Cr oxidation is limited to a few percents, and uniform in the film. Cr on MgO presents a well-ordered tetragonal structure with a 45° degree rotation of the lattice (Cr[100]||MgO[110]), able to minimize the lattice mismatch and resulting in a relatively small in-plane biaxial tensile strain. By adjusting the film thickness (from 10 nm to 50 nm) and the post-annealing temperature (up to 873 K), the elastic energy accumulated within the lattice can be partially relaxed through edge dislocations. Consequently, the lattice parameters can be finely tuned (from 0.2944 nm to 0.2897 nm in-plane, and from 0.2867 nm to 0.2886 nm out-of-plane), eventually approaching bulk chromium values (0.2885 nm, cubic). The control over the film stress via thickness and/or annealing temperature could be potentially exploited to tune the Néel temperature of the antiferromagnet, extending the device capability to different temperature ranges.

Finally, we demonstrate the epitaxy of Pt thin films over Cr/MgO. Grown by molecular beam epitaxy at room temperature, the platinum film presents a high crystal order, with a 45° degree rotation of the lattice (Cr[100]||Pt[110]), and does not affect the chemical and structural properties of the Cr layer underneath. These results finally pave the way to the exploitation of Cr/MgO and Pt/Cr/MgO systems for Cr-based spintronics applications suggested by recent works [39,40].

ACKNOWLEDGEMENTS

We thank R. Bertacco, X. Marti, I. Fina, and J. Železný for valuable discussion, S. Bertoli and M. Di Loreto for their support on the experimental activity. This work was performed at Polifab, the

micro and nanofabrication facility of Politecnico di Milano.

SUPPLEMENTARY MATERIAL

See supplementary material for: (S1) the Electron Energy Loss Spectroscopy characterization of sample C50A; (S2) the Low Energy Electron Diffraction investigation of sample C50A, as-grown and with an MgO capping layer; (S3) the morphology of C50 and C50A samples imaged by Atomic Force microscopy; (S4) the X-ray Reciprocal Space Mapping of C10, C25, C50, C50a, C50A, P10, P50, and P50A samples; (S5) the high-resolution Transmission Electron Microscope imaging of an interface dislocation at the Cr/MgO interface in sample C50A; (S6) the comparison between X-ray Photoemission Spectroscopy spectra from C2A and P2A samples; (S7) the schematic structure of the Pt/Cr/MgO lattice stacking.

REFERENCES

[1] Jungwirth T, Martì X, Wadley P and Wunderlich J 2016 *Nat. Nanotech.* **11** 231
[2] Gomonay E V and Loktev V M 2014 *Low Temp. Phys.* **40** 17
[3] Seifert T *et al.* 2016 *Nat. Photonics* **10** 483.
[4] Bertacco R and Cantoni M 2016 New Trends in Magnetic Memories *Ultra-high-density magnetic recording: storage materials and media designs* ed Pan Stanford p 457
[5] Baltz V, Manchon A, Tsoi M, Moriyama T, Ono T and Tserkovnyak Y 2018 *Rev. Mod. Phys.* **90** 015005
[6] Scholl A, Liberati M, Arenholz E, Ohldag H and Stohr J 2004 *Phys. Rev. Lett.* **92** 247201
[7] Petti D *et al* 2013 *Appl. Phys. Lett.* **102** 192404
[8] Sapozhnik A A, Abrudan R, Skourski Y, Jourdan M, Zabel H, Kläui M and Elmers H J 2017 *Rapid Research Letters* **11** 1600438
[9] Reichlova H *et al.* 2015 *Phys. Rev. B* **92** 165424
[10] Kosub T *et al.* 2017 *Nat. Comm.* **8** 13985
[11] van der Brink A, Vermijs G, Solignac A, Koo J, Kohlhepp J T, Swagten H J M and Koopmans B 2016 *Nat. Comm.* **7** 10854
[12] Marti X *et al.* 2014 *Nature Mat.* **13** 367
[13] Park B G *et al.* 2011 *Nature Mat.* **10** 347
[14] Frangou L, Oyarzún S, Auffret S, Vila L, Gambarelli S and Baltz V 2016 *Phys. Rev. Lett.* **116** 077203
[15] Albisetti E *et al.* 2018 *Communications Physics* **1** 56
[16] Barthem V M T S, Colin C V, Mayaffre H, Julien M H and Givord D 2013 *Nature Comm.* **4** 2892
[17] Wu H C *et al.* 2016 *Adv. Funct. Mat.* **26** 5884
[18] Wadley P *et al.* 2013 *Nature Commun.* **4** 1
[19] Wadley P *et al.* 2016 *Science* **5** 587
[20] Fina I *et al.* 2014 *Nature Comm.* **5** 4671
[21] Muir W B and Strom-Olsen J-O 1971 *Phys. Rev. B* **4** 988

[22] Fawcett E 1988 *Rev. Mod. Phys.* **60** 210
[23] http://pubs.usgs.gov/fs/2002/fs087-02
[24] Kummamuru R K and Soh Y A 2008 *Nature* **452** 859
[25] Leroy M A, Bataille A M, Bertran F, Le Fèvre P, Taleb-Ibrahimi A and Andrieu S 2013 *Phys. Rev. B* **88** 205134
[26] Wang C M, Kaspar T C, Shutthanandan V, Joly A G and Kurtz R J 2011 *Acta Materialia* **59** 4274
[27] Sawabu M, Ohashi M, Ohashi K, Miyagawa M, Kubota T and Takanashi K 2017 *J. of Phys: Conf. Series* **871** 012002
[28] Hanf M C, Pirri C, Peruchetti J C, Bolmont D and Gewinner G 1989 *Phys. Rev. B* **39** 1546
[29] Krembel C, Hanf M C, Peruchetti J C, Bolmont D and Gewinner G 1991 *Phys. Rev.B* **44** 8407
[30] Riva M, Picone A, Bussetti G, Brambilla A, Calloni A, Berti G, Duò L, Ciccacci F and Finazzi M 2014 *Surf. Sci.* **621** 55
[31] Leroy M A *et al.* 2014 *Phys. Rev. B* **90** 035432
[32] Fu Q and Wagner T 2002 *Thin Solid Films* **420-421** 455
[33] Fu Q and Wagner T 2005 *J. Phys. Chem. B* **109** 11697
[34] Wagner T, Fu Q, Winde C, Tsukimoto S and Phillipp F 2004 *Interface Sci.* **12** 117
[35] Sonntag P, Bodeker P, Brohl K, Thurston T and Zabel H 1997 *Nuclear Instrument and Methods in Physics Research B* **97** 468
[36] Hill J P, Helgesen G and Gibbs D 1995 *Phys. Rev. B* **51** 10336
[37] Mattson J, Brumitt B, Brodsky M B and Ketterson J B 1990 *J. Appl. Phys.* **67** 4889
[38] Ohashi M, Ohashi K, Sawabu M, Miyagawa M, Kubota T and Takanashi K 2016 *Phys. Lett. A* **380** 3133
[39] Asa M, Autieri C, Pazzocco R, Rinaldi C, Brzezicki W, Stroppa A, Cuoco M, Picozzi S and Cantoni M 2019 arXiv:1904.03541; 2019 *Phys. Rev. Lett.* submitted
[40] Bragato M, Achilli S, Cargnoni F, Ceresoli D, Martinazzo R, Soave R and Trioni M I 2018 *Materials* **11** 2030
[41] McIntyre P C, Maggiore C J and Nastati M 1997 *Acta Mater.* **45** 879
[42] Bertacco R, Cantoni M, Riva M, Tagliaferri A and Ciccacci F 2005 *Appl. Surf. Sci.* **252** 1754
[43] Bolef D I and de Klerk J 1963 *Phys. Rev.* **129** 1063
[44] Hart J L, Lang A C, Leff A C, Longo P, Trevor C, Twesten R D and Taheri M L 2017 *Scientific Reports* **7**, 8243
[45] Biesinger M C, Payne B P, Grosvenor A P, Lau L W M, Gerson A R and Smart R St.C 2011 *Appl. Surf. Science* **257** 2717
[46] Tanuma S, Powell C J and Penn D R 1991 *Surf. Interface Anal.* **17** 911
[47] Asa M *et al.* 2018 *Phys. Rev. Materials* **2** 034401
[48] The corresponding angles, calculated employing the simple atomic scheme in the inset, are 26.6° and 45° assuming a cubic cell, that is $a_{\perp}/a_{//} = 1$.
[49] Note that this analysis was performed *in-situ* on the same sample. First, 2 nm of Cr were grown (C2); then, 48 nm of Cr were added (C50); finally, the film was annealed to 873 K (C50A). After each step an XPD was measured. This procedure allowed a more reliable comparison to be obtained by reducing errors due to e.g. substrate mounting or cleaning.
[50] Fawcett E, Feder D, Muir W C and Vettier C 1984 *J. Phys. F: Met. Phys.* **14** 1261
[51] Marcinkowski M J and Lipsitt H A 1961 *J. Appl. Phys.* **32** 1238
[52] Miron I M, Gaudin G, Auffret S, Rodmacq B, Schuhl A, Pizzini S, Vogel J and Gambardella P 2010 *Nat. Mat.* **9** 230
[53] Emori S, Bauer U, Ahn S-M, Martinez E and Beach G S D 2013 *Nat. Mat.* **12** 611
[54] Kosub T, Kopte M, Radu F, Schmidt O G and Makarov D 2015 *Phys. Rev. Lett.* **115** 097201
[55] Baldrati L *et al.* 2018 *Phys. Rev. B* **98** 024422
[56] The different shape of the XPD curve of the Pt-capped film with respect to the uncapped film (empty and full black dots, respectively) is mainly ascribed to the attenuation of the Cr signal due to the Pt overlayer, larger at low angles and smaller at high angles.
[57] Note that the measured values come from the parallel of the Cr and Pt layers. Anyway, considering that the Pt layer is much thinner than the Cr layer, and that the bulk resistivities of both are almost identical, the reported value can be considered a good approximation of the Cr resistivity only.